ADVANCED FUNCTIONAL MATERIALS
www.afm-journal.de

Spiro Linkage as an Alternative Strategy for Promising Nonfullerene Acceptors in Organic Solar Cells

Xiao-Feng Wu, Wei-Fei Fu, Zheng Xu, Minmin Shi, Feng Liu, Hong-Zheng Chen,* Jun-Hua Wan,* and Thomas P. Russell*

This work focuses on developing diketopyrrolopyrrole (DPP)-based small molecular nonfullerene acceptors for bulk heterojunction (BHJ) organic solar cells. The materials, SF-DPPs, have an X-shaped geometry arising from four DPP units attached to a spirobifluorene (SF) center. The spiro-dimer of DPP-fluorene-DPP is highly twisted, which suppresses strong intermolecular aggregation. Branched 2-ethylhexyl (EH), linear *n*-octyl (C8), and *n*-dodecyl (C12) alkyl sides are chosen as substituents to functionalize the *N*,*N*-positions of the DPP moiety to tune molecular interactions. SF-DPPEH, the best candidate in SF-DPPs family, when blended with poly(3-hexylthiophene) (P3HT) showed a moderate crystallinity and gives a J_{sc} of 6.96 mA cm^{-2}, V_{oc} of 1.10 V, a fill factor of 47.5%, and a power conversion efficiency of 3.63%. However, SF-DPPC8 and SF-DPPC12 exhibit lower crystallinity in their BHJ blends, which is responsible for their reduced J_{sc}. Coupling DPP units with SF using an acetylene bridge yields SF-A-DPP molecules. Such a small modification leads to drastically different morphological features and far inferior device performance. These observations demonstrate a solid structure–property relationship by topology control and material design. This work offers a new molecular design approach to develop efficient small molecule nonfullerene acceptors.

1. Introduction

Bulk-heterojunction (BHJ) organic solar cells (OSCs) were intensively studied over the past 20 years in fabricating lightweight, flexible, and cost-effective thin film solar cells. Most work in materials design has focused on developing donor polymers[1] and small molecules.[2] Electron acceptors are as important as the electron donors to achieve high performance OSCs and their development has lagged behind. Fullerene derivatives are the leading electron acceptors in OSCs, due to their good electron accepting properties and isotropic electron mobility, benefiting from the large spherical conjugated π-electron system.[3] Bicontinuous and phase-separated morphologies with domains tens of nanometers in size can be obtained by thermal/solvent treatment.[4] However, fullerenes do not significantly contribute to light harvesting at wavelengths greater than 600 nm,[5] and their energy levels cannot be fine-tuned to match the donor materials to maximize the open-circuit voltage (V_{oc}) and minimize the energy loss.[6] Moreover, fullerenes are not an ideal material for production on an industrial scale despite the successes in laboratory scale devices.[7] For these reasons, nonfullerene acceptor materials including small molecules[8] and conjugated polymers[9] have been intensively pursued lately, using strong electron-withdrawing groups such as cyano,[10] imide and amide,[11] benzothiadiazole,[12] diketopyrrolopyrrole (DPP)[13] to fine-tune energy levels. Poly(3-hexylthiophene) (P3HT) is often used as a model donor material to investigate performance of donor materials, and most recent report showed power conversion efficiencies (PCEs) exceeding 3%.[12f,13h,14]

Small molecules (SM) with planar structure tend to form excessively large crystalline domains.[11e,15] To minimize the formation of such unfavorably large crystalline domains, SM acceptors with twisted structures or with bulky bridging units have been developed.[11a,11d,15b] Recent studies demonstrated that PDI dimers with twisted structures showed promising performance as electron acceptors in solution-processed OSCs due to the significant reduction in aggregation.[16] However, unlike fullerenes that isotropically transport charge, the charge transport of PDI dimers is still highly anisotropic, with high mobility along the π-stacking direction.[17] A common strategy

X.-F. Wu, Dr. Z. Xu, Dr. J.-H. Wan
Key Laboratory of Organosilicon Chemistry and Material Technology of Ministry of Education
Hangzhou Normal University
Hangzhou 310012, P. R. China
E-mail: wan_junhua@hznu.edu.cn
Dr. W.-F. Fu, Prof. M. Shi, Prof. H.-Z. Chen
State Key Laboratory of Silicon Materials
MOE Key Laboratory of Macromolecular Synthesis and Functionalization
Department of Polymer Science and Engineering
Zhejiang University
Hangzhou 310027, P. R. China
E-mail: hzchen@zju.edu.cn
Dr. F. Liu
Materials Sciences Division
Lawrence Berkeley National Laboratory
Berkeley, CA 94720, USA
E-mail: iamfengliu@gmail.com
Prof. T. P. Russell
Polymer Science and Engineering Department
University of Massachusetts
Amherst, MA 01003, USA

DOI: 10.1002/adfm.201502413

of constructing nonplanar conjugated electron acceptors with 3D structure is to introduce a star-shape core into the *n*-type molecules. Only a few star-shape cores have been used up to now, for example, triphenylamine (TPA),[18] tetraphenylethylene (TPE),[15a] [2,2]paracyclophane,[13g] azadipyrromethene,[14b] and tetraphenylsilane(methane).[19]

DPP-based materials exhibited high electron mobilities due to their low-lying lowest unoccupied molecular orbital (LUMO) energy levels.[20] Therefore, many DPP-based materials have been recently developed as electron acceptors for OSCs. Simple DPP acceptors provided low PCEs (<1.2%) despite the high V_{oc}.[13a–e] Encouragingly, silafluorene-based bis-DPP electron acceptors gave PCE as high as 2%.[13f] Very recently, the efficiency has been improved to exceed 3% by replacing the central 2-ethylhexyl-modified silafluorene unit with 9,9-dipropylfluorene.[13h]

Here, we report a new synthetic strategy to convert planar subunits to highly twisted SM acceptors by introducing a spiro-linkage, using spirobifluorene (SF). Coupling the SF core with four rigid DPPs yielded a new series of nonplanar DPP-based acceptors (**SF-DPP**, **Figure 1**a). SF was chosen among the known nonplanar and star-shaped cores based on the following considerations: Firstly, the orthogonal arrangement of the two fluorene units is fixed, where modification can lead to new materials with high nonplanarity that weakens intermolecular interactions[21]; Second, sp^3-hybridized C-bridge in the SF center will block electron transfer within the DPP-fluorene-DPP substructure and the designed acceptor is actually a spiro dimer of DPP-fluorene-DPP building block. Notably, Zhao and co-workers had utilized spirobifluorene-2,7-diyl linker to construct a PDI dimmer (**SF-PDI$_2$**) acceptor in which one half of the SF core is an unsubstituted fluorene unit.[15b] Interestingly, Yan and co-workers recently described that high-performance nonfullerene OSCs were achieved with **SF-PDI$_2$** as acceptor by the combination of a difluorobenzothiadizole donor polymer.[22] Branched 2-ethylhexyl (EH), linear *n*-octyl (C8) and n-dodecyl (C12) alkyl substituents were used, yielding three molecular variants, **SF-DPPEH**, **SF-DPPC8**, and **SF-DPPC12**. For comparison, another new series of acceptors (**SF-A-DPP**) were also synthesized by introducing C–C triple bond to link SF core and DPP units, yielding **SF-A-DPPEH**, **SF-A-DPPC8**, and **SF-A-DPPC12** (Figure 1c). A detailed investigation of their photophysical, electrochemical, and thermal properties was performed. These materials have been investigated as acceptor material to fabricate BHJ cells using P3HT as the electron donor. A combination of X-ray diffraction and scattering techniques have been

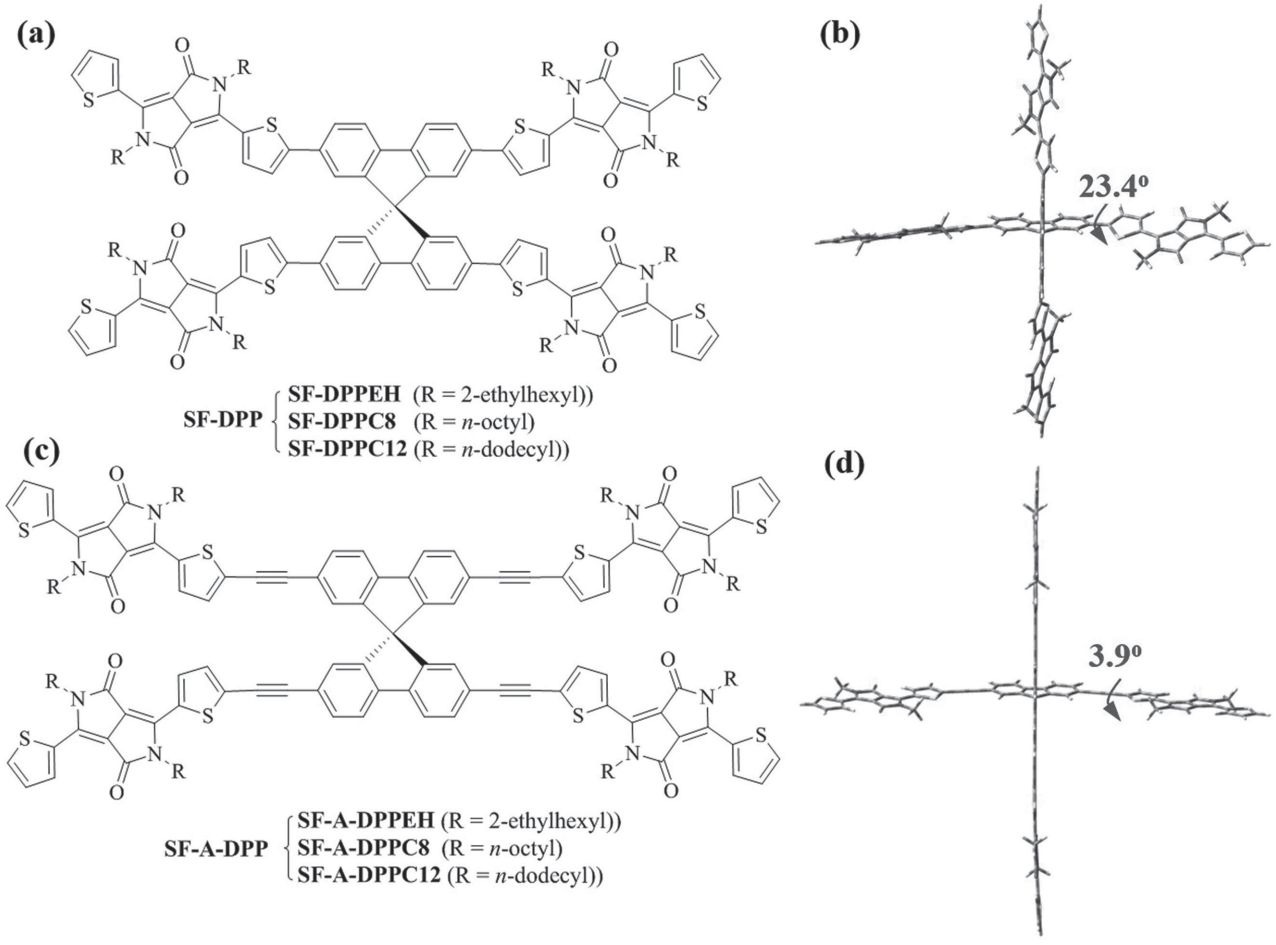

Figure 1. The chemical structure of novel SM acceptors, a) **SF-DPP** and c) **SF-A-DPP** series. Ground-state geometries of methyl analogues of b) **SF-DPP**, and d) **SF-A-DPP**, as calculated from density functional theory.

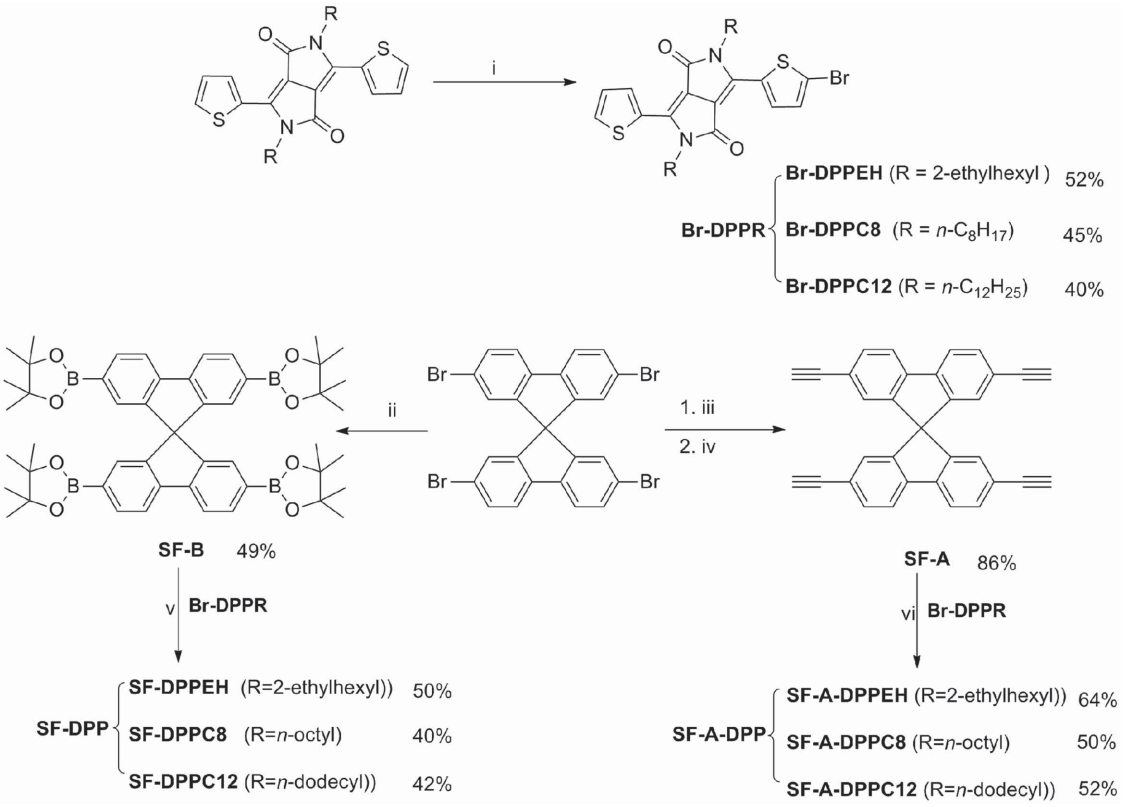

Scheme 1. The synthetic route for **SF-DPP** and **SF-A-DPP** molecules. i) NBS/$CHCl_3$, 0 °C, overnight; ii) bis(pinacolato)diboron, $Pd(dppf)Cl_2$, KOAc, dioxane, 80 °C, 24 h; iii) trimethylsilylacetylene, $Pd(PPh_3)_2Cl_2$, CuI, PPh_3, *i*-Pr_2NH, 80 °C, 24 h; iv) NaOH/CH_3OH, CH_2Cl_2, rt, 6 h; v) $Pd(PPh_3)_4$, toluene, 85 °C, 48h; vi) $Pd(PPh_3)_4$, *i*-Pr_2NH/toluene, 85 °C, 48 h.

used to investigate how the alkyl chains on the new acceptors influence the crystallinity and morphology of the BHJ films.

2. Result and Discussion

2.1. Synthesis and Characterization

The synthesis of the **SF-DPP**s and **SF-A-DPP**s involves the synthesis of two key intermediate compounds, four boronic ester and acetylene modified SF derivatives, respectively. **Scheme 1** shows the synthetic route to converting of 2,2′,7,7′-tetrabromo-9,9′-spirobifluorene into corresponding tetraboronic acid pinacol ester (**SF-B**) and tetraacetylene derivatives (**SF-A**). Both tetra-substituted derivatives were obtained with high yield, especially for the latter (above 90%). Further Suzuki coupling reaction between **SF-B** and monobrominated diketopyrrolopyrrole (**Br-DPPR**) at a molar ratio of 1:6 afforded the desired four-arm X-shaped molecules, **SF-DPP** (**SF-DPPEH**, **SF-DPPC8**, and **SF-DPPC12**) in moderate yields (40%–50%). Sonagashira condensation of **SF-A** and 6 eq corresponding **Br-DPP** compound achieved the **SF-A-DPP** series with good yields (50%–64%). The target small molecules were fully characterized by ^1H and ^{13}C NMR spectroscopy, MALDI-TOF-MS and high-resolution mass spectrometry. All **SP-DPP** and **SF-A-DPP** molecules are soluble in common organic solvents such as CH_2Cl_2, $CHCl_3$, tetrahydrofuran (THF), toluene, chlorobenzene, and dichlorobenzene.

2.2. Molecular Geometry

Optimized ground state geometry spiro-DPP acceptors were calculated using Gaussian 09 software package at the B3LYP/6-31G (d, p) level of theory in the gas phase using density functional theory (DFT). In the calculations, the alkyl side chains of the molecules were replaced by methyl groups to reduce machine time. As shown in Figure 1b,d, the SF core in both **SF-DPP** and **SF-A-DPP** models is perfectly cruciform with two orthogonal conjugated backbones. In the **SF-DPP** model, DPP moieties are twisted out of the connected fluorene plane of SF core with interplanar angle of 23.4°. And as expected, in the **SF-A-DPP** model, DPP units lie nearly in the plane of fluorene with interplanar angle of only 3.9° due to very low barrier for the rotation around C–C triple bond. The cruciform X-shape of these molecules can help to avoid strong crystalline packing.

2.3. Thermal Properties

Thermogravimetric analysis (TGA) and differential scanning calorimetry (DSC) in a nitrogen atmosphere were performed to investigate the thermal properties of these new acceptors. The 5% weight-loss temperatures (T_d) of **SF-DPPEH**, **SF-DPPC8,** and **SF-DPPC12** are 402, 375, and 280 °C, respectively (see Figure S1, Supporting Information), indicating that branched alkyl chain is more beneficial for stabilizing materials than

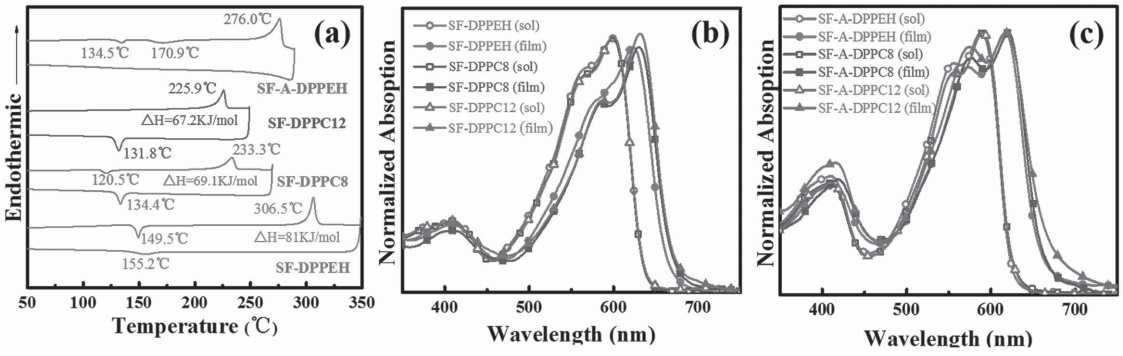

Figure 2. a) DSC thermograms at 10 min^{-1} for **SF-DPPs** and **SF-A-DPPEH** in the different temperature range. UV–vis absorption spectra of b) **SF-DPP**s and c) **SF-A-DPP**s in CH_2Cl_2 solutions and in solid films on the quartz plate.

linear chains in **SF-DPPs**. However, all three **SF-A-DPP** acceptors showed almost the same weight-loss temperature with a T_d of about 300 °C. All compounds are thermally stable enough to be used in solar cells.

Figure 2a shows the DSC traces of **SP-DPPs** and **SF-A-DPPEHs**. These compounds showed crystalline melting temperature (T_m) ranging from 225 to 307 °C. 2-Ethylhexyl substituted **SF-DPPEH** (T_m = 306.5 °C) showed considerably increased melting temperature in comparison to its analogues bearing linear *n*-octyl side chains (**SF-DPPC8**, T_m = 233.3 °C). And T_m decreases as the length of the linear alkyl chain increases from 8 to 12. A small exothermic peak occurs, around 149.5 °C for **SF-DPPEH** and 120.5 °C for **SF-DPPC8**, respectively, before the melting endothermic peak, as a result of cold crystallization of the amorphous molecules,[23] which promotes the aggregation of both alkyl side chains and molecular backbone. Based on the comparison of the melting enthalpy values ΔH (KJ/mol) for the phase-transition, one can find that the degree of crystallinity for **SF-DPPEH** is higher than that of **SF-DPPC8** and **SF-DPPC12**. Upon cooling, both **SF-DPPC8** and **SF-DPPC12** exhibited crystallization exotherms at 133.4 and 131.8 °C, respectively. **SF-A-DPPEH** exhibits two cold crystallization processes (134.5 and 170.9 °C), with a pronounced melting transition at 276 °C. The DSC findings explain that both the alkyl side chains (such as structure and length)[24] and linkage between two connected π moieties in conjugated backbone are integral to intermolecular forces, thereby modulating T_m and T_c.

2.4. Optoelectronic Properties

The optoelectronic properties of **SF-DPPs** and **SF-A-DPPs** were characterized using UV–vis absorption. Figure 2b,c shows the absorption spectra of molecules in dilute CH_2Cl_2 solutions and in thin films, and the corresponding data are summarized in **Table 1**. In CH_2Cl_2 solution, all acceptor molecules showed two distinct absorption bands including a weak band in the shorter wavelength region (300–400 nm) and a strong band with typical vibronic structure[25] in the longer wavelength region (450–650 nm). The longer wavelength absorption originating from the intramolecular charge transfer (ICT) is associated with the DPP. Moreover, the introduction of C–C triple bonds results in only slightly blue-shifted (<10 nm), as shown in **SF-A-DPP**s. The maximum absorption coefficients (ε_{max}) of the three **SF-DPP** molecules were in the range of (1.75–1.78) × 10^5 M^{-1} cm^{-1}, which was a slightly higher than those (1.51–1.58 × 10^5 M^{-1} cm^{-1}) of the **SF-A-DPP** molecules. In addition, the same absorption spectra in solution confirmed that the electronic structure was nearly independent of the alkyl side chains for each series of molecules. In thin films, all six molecules exhibited a red-shift (26–33 nm) in absorption, suggesting enhanced π–π interactions. The optical band gaps of films are ≈1.7–1.8 eV, estimated from the absorption edges.

Cyclic voltammetry (CV) experiments were carried out to investigate electronic structure of **SF-DPP** and **SF-A-DPP** molecules. Experiments were done in CH_2Cl_2 solution (**Figure 3**). As

Table 1. Optical and electrochemical properties of **SF-DPP**s and **SF-A-DPP**s.

Compound	UV–vis absorption				Cyclic voltammetry		
	λ_{max}^{sol} [nm]	$\varepsilon(\lambda_{max}^{sol})$ [M^{-1} cm^{-1}]	λ_{max}^{film} [nm]	E_g^{opt} [a)] [eV]	HOMO [eV]	LUMO [eV]	E_g^{cv} [b)] [eV]
SF-DPPEH	597	1.78 × 10^5	622	1.79	−5.26	−3.60	1.66
SF-DPPC8	598	1.75 × 10^5	629	1.78	−5.24	−3.55	1.69
SF-DPPC12	597	1.78 × 10^5	631	1.75	−5.23	−3.57	1.66
SF-A-DPPEH	588	1.58 × 10^5	616	1.81	−5.30	−3.58	1.72
SF-A-DPPC8	590	1.57 × 10^5	620	1.81	−5.29	−3.56	1.73
SF-A-DPPC12	590	1.51 × 10^5	618	1.76	−5.29	−3.57	1.72

[a)]Optical band gap derived from absorption onset of films; [b)]Band gap derived from the difference between highest occupied molecular orbital (HOMO) and LUMO energy levels.

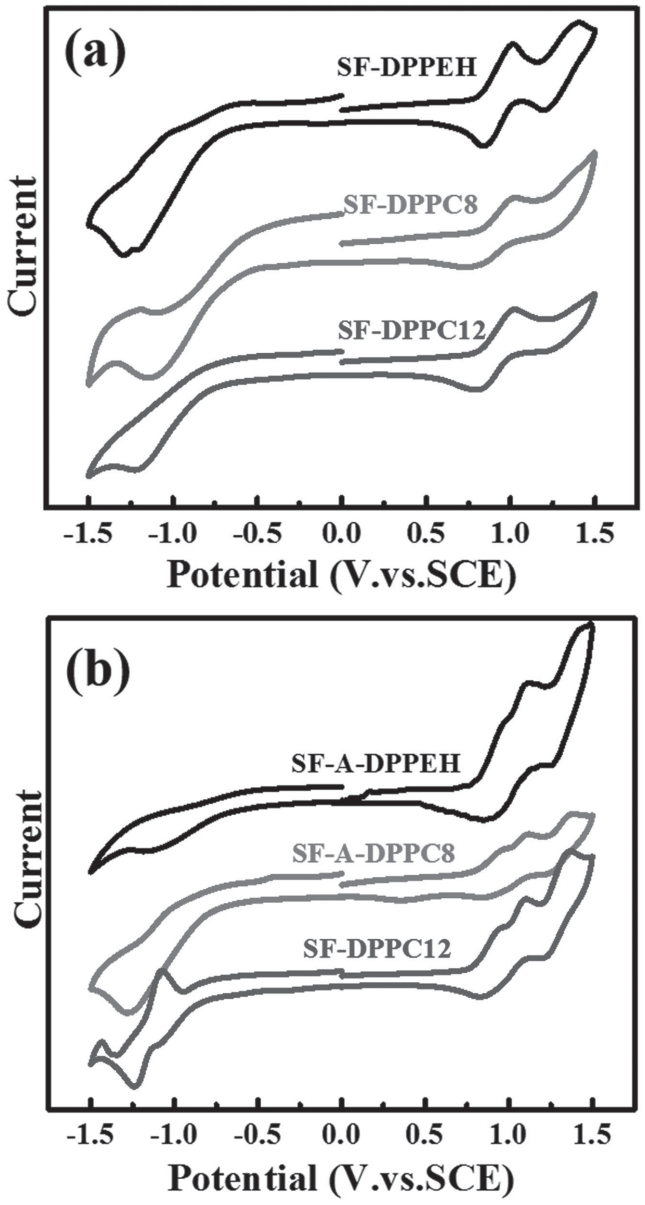

Figure 3. Electrochemical cyclic voltammetry of the six acceptors in CH_2Cl_2 solution with the SCE reference electrode. Scan rate: 100 mV s^{-1}.

shown in Figure 3, all molecules undergo reversible multiple-electron oxidations originating from successive oxidation of the different DPP moieties. However, **SF-DPPEH**, **SF-A-DPPC8**, and **SF-A-DPPC12** exhibit one or two quasi-reversible reductions and an irreversible reduction was observed for other molecules. The onset potential of a ferrocene/ferrocenium (Fc/Fc+) redox couple was found to be 0.34 V referencing to the SCE electrode in our measurement system, and the energy level of Fc/Fc+ was assumed to be at –4.8 eV under vacuum.[26] The HOMO and LUMO energy levels of compounds in solution can be estimated from the equation of HOMO/LUMO = –exp(*E*(ox/re) + 4.46) (eV). The HOMO/LUMO levels for all six acceptors were listed in and Table 1. Compared with **SF-DPP**, the HOMO of **SF-A-DPP** is slightly lower, demonstrating that C–C triple bond herein has minor influence on the both HOMO/LUMO energy levels.

These LUMO levels were higher (≈0.2–0.3 eV) than the corresponding value of $PC_{61}BM$ estimated to be ≈–3.84 eV,[12f] indicating that V_{oc} in devices prepared using these compounds was expected to exceed that of $PC_{61}BM$ acceptor devices. Based on the HOMO/LUMO energy levels of P3HT (–4.94/–2.94 eV),[27] the energy offsets (ΔE_{LUMO}) between the LUMO of P3HT and those of the new acceptors is above 0.6 eV. While the relative HOMO offsets (ΔE_{HOMO}) is above 0.3 eV and the substantially ΔE_{LUMO} strongly suggests that blending P3HT with **SF-DPP** or **SF-A-DPP** acceptor, the resulted active layer blends would apply electron transfer from LUMO of P3HT to LUMO of these DPP-based acceptors as the mechanism for producing free electrons and holes.[12e]

2.5. Nonfullerene Organic Solar Cells

Spiro-DPPs acceptors were used in bulk heterojunction solar cells, pairing P3HT as the donor material. OSCs were fabricated with the configuration of ITO/PEDOT:PSS/P3HT:**SF-DPP** or **SF-A-DPP**/PFN/Al and tested under simulated 100 mW cm^{-2} AM 1.5G illumination. First, we performed the optimization of photovoltaic performance of the OSCs of P3HT:**SF-DPP** blends by changing the D/A weight ratios. The details on the effects of the blend ratios, the annealing process and the annealing temperature are provided in the Supporting Information (Table S1, Supporting Information). The device performance parameters for the three blends under the optimized fabrication conditions were summarized in **Table 2**. The current density–voltage (*J*–*V*) characteristics of the optimized devices were presented in **Figure 4**a. Interestingly, the OSCs involving the blends of the three different **SF-DPP** acceptors showed large variations in photovoltaic performance. The highest PCE of 3.63% was obtained from a P3HT:**SF-DPPEH** (1:1) upon thermal annealing at 120 °C for 10 min. P3HT:**SF-DPPC8** and P3HT:**SF-DPPC12** blend films under the same D/A weight ratio (1:1) led to the best photovoltaic performance upon post-annealing at 100 °C for 10 min, with PCE of 1.87% and 1.42%, respectively. The OSCs fabricated from three different **SF-A-DPP** acceptors were optimized on the basis of the same optimal D/A weight ratios (1:1). The three best **SF-A-DPP**-based devices exhibited low photovoltaic performance with a PCE of 0.76% for P3HT:**SF-A-DPPEH** and below 0.5% for both P3HT:**SF-A-DPPC8** and **SF-A-DPPC12** blends.

Table 2. Photovoltaic performance of the best nonfullerene solar cells.

Acceptors	Annealing Temp. [°C]	V_{oc} [V]	J_{sc} [mA cm^{-2}]	FF	PCE [%]
SF-DPPEH	120	1.10	6.96	47.5	3.63
SF-DPPC8	100	0.88	5.21	40.9	1.87
SF-DPPC12	100	0.91	3.88	40.1	1.42
SF-A-DPPEH	140	0.75	2.37	42.6	0.76
SF-A-DPPC8	w/o	0.79	1.21	28.9	0.28
SF-A-DPPC12	w/o	0.70	1.96	33.1	0.45

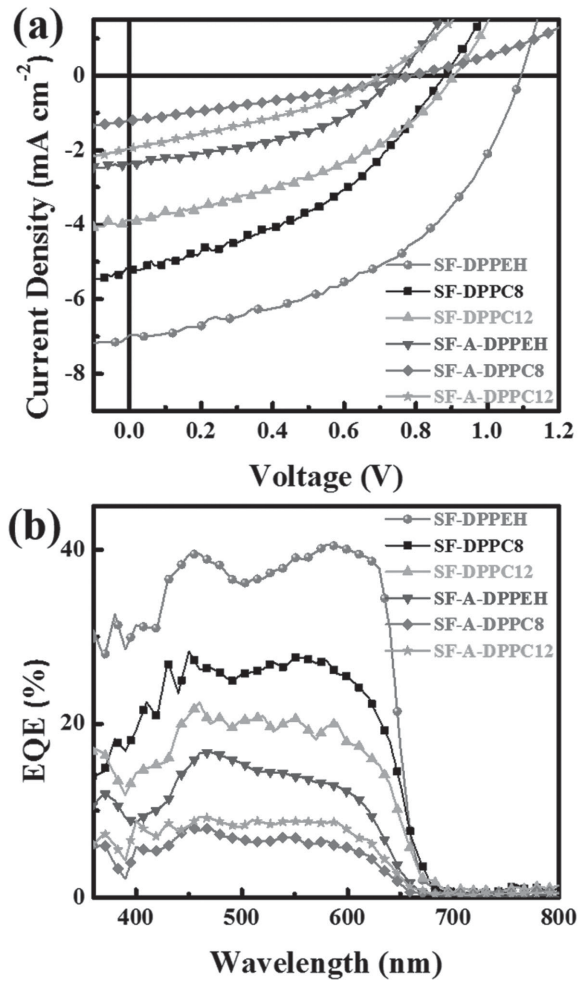

Figure 4. a) *J–V* curves and b) external quantum efficiency (EQE) curves of the best nonfullenrene devices of the six spiro-DPP acceptors when blended with the donor polymer P3HT.

Similar to other DPP-based acceptors,[13h,18a] a high V_{oc} (1.10 eV) was obtained for the P3HT:**SF-DPPEH** blend, which was mainly due to the large energy level offset (1.34 eV) between the HOMO (–4.94 eV) of P3HT and the LUMO (–3.60 eV) of **SF-DPPEH**. Although there was only a small difference in the LUMOs among the three **SF-DPP** acceptors, the V_{oc} of the linear alkyl chain acceptor (**SF-DPPC8** and **SF-DPPC12**)-based devices showed reduction in V_{oc} (≈0.9 V). We thought that there were other influential factors besides the HOMO–LUMO gaps that play a role in determining the V_{oc}[28] (see Section 2.6). When compared the best devices prepared using **SF-DPP** and **SF-A-DPP** acceptors, one can find that the V_{oc} obtained with the former was significantly higher than that obtained from the latter. Additionally, the higher light absorption and lower bandgap of **SF-DPP** acceptors also contributes to their higher J_{sc}.

The major advantage of nonfullerene acceptor is their light absorption. We investigated how acceptor materials were involved in exciton formation. **Figure 5** shows the absorption spectra of the blending thin films of P3HT:**SF-DPP** at weight ratios of 1:1, before and after thermal annealing. Before annealing, all three P3HT:**SF-DPP** thin films absorb in the range of 300–680 nm with two clear absorption peaks, the absorption peaks at longer wavelengths (620 nm) derived from the **SF-DPP** acceptor and the absorption peaks at shorter wavelength (566 nm) originated from the P3HT. There was a considerable enhancement in their absorptions upon thermal annealing. For **SF-DPPEH**-based film, absorption increased by about 25%. More interestingly, thermal annealing made the two absorption bands stronger and more resolved, demonstrating enhanced crystallinity for both components. However, for other blends, enhancement was seen only in the 566 nm absorption, arising from the improved crystallinity, only for P3HT.

The external quantum efficiencies (EQEs) of the best devices, as well as the overlap between the EQE of P3HT:**SF-DPPEH** blend and absorption of pure P3HT and **SF-DPPEH** films, are shown in Figure 4b and Figure 5d, respectively. In Figure 4b, it can be seen that the EQEs spectra of the best devices based on **SF-DPP** acceptors showed an effective photoconversion efficiency within a similar wavelength range from 300 to 680 nm, which is a little broader range when compared to those (300–650 nm) of **SF-A-DPP**s-based devices. From the overlapped spectra (Figure 5d), it is obvious that **SF-DPPEH** contributed to the harvesting of light from 600 to 680 nm. **SF-DPP**s blend films also showed higher EQE spectra than **SF-A-DPP**s blend films, in agreement with their high J_{sc} values in the devices. **SF-DPPEH**-based devices had the highest conversion efficiencies at all wavelengths with EQEs between 36.5% and 40% throughout the 400–650 nm range, with a peak EQE of 41% attained at 590 nm. Note that the electronic structure of **SF-DPP** acceptors is independent of the alkyl side chains and the difference of device performances originated from the difference in morphology in the blended thin film, which will be discussed in detail in the following section.

Photoluminescence quenching was used to estimate charge separation and recombination in the active layers. The pristine film of P3HT strongly fluoresced, while the fluorescence of all pure acceptors films was very weak (data not shown). The PL spectra of the pristine film of the P3HT and their blends were shown in Figure S5, Supporting Information. Obviously, each acceptor almost entirely quenched the fluorescence of P3HT in blend films. Quenching efficiencies of 83%, 92%, and 91% were measured for the P3HT:**SF-DPPEF**, 3HT:**SF-DPPC8**, and P3HT:**SF-DPPC12** blend films, respectively. Further, quenching efficiencies of 85%, 95%, and 89% were observed for P3HT:**SF-A-DPPEH**, P3HT:**SF-A-DPPC8**, and P3HT:**SF-A-DPPC12** blends, respectively. According to the forgoing discussion about the mechanism for exciton dissociation, here, quenching of the P3HT fluorescence came mainly from the electron transfer from P3HT to acceptor. Such high quenching efficiencies suggest that excitons in each of the blends travel to the donor:acceptor interface and are separated with high efficiency. Among the six blends, P3HT:**SF-DPPEH** blend film with the highest efficiency, but with the lowest quenching efficiency. The discrepancy is mainly as a result of the differences in morphology. In addition, the remaining spectral shape of the emission from the blend of P3HT and **SF-DPPEH** is similar to that of pure P3HT. This is due to the trances of large P3HT domains whose dimensions exceed the exciton diffusion length, thus the excitons in this domains decay before reaching

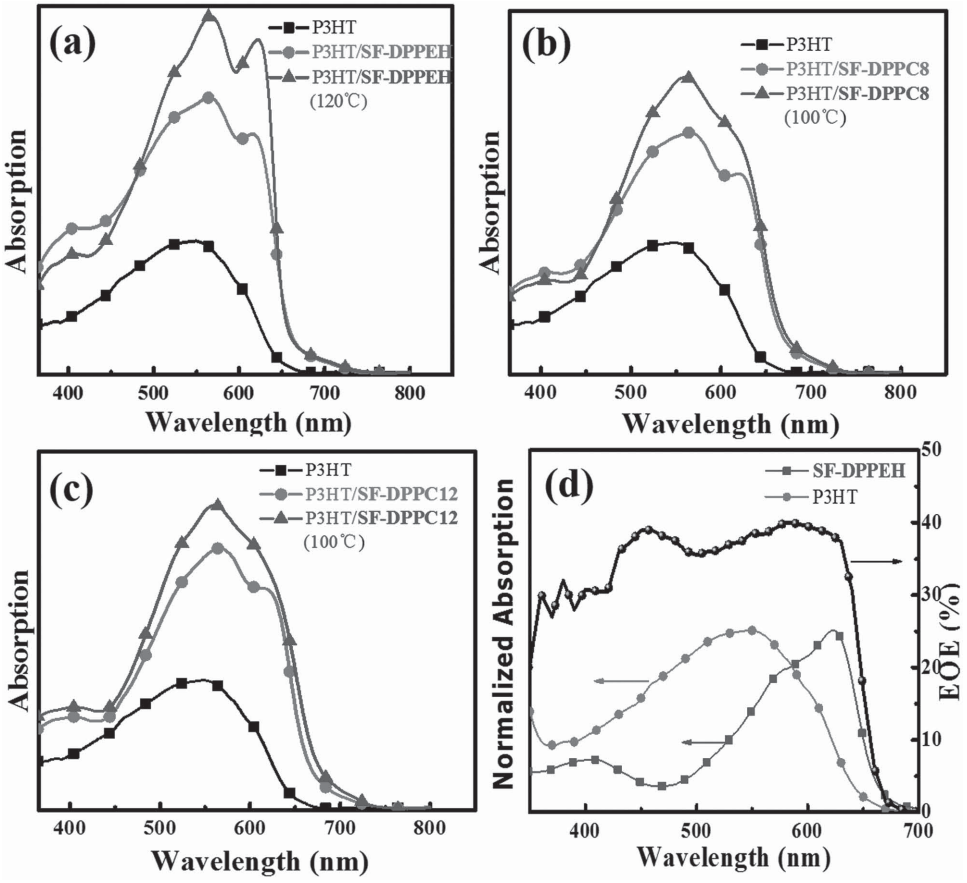

Figure 5. a–c) UV–vis absorption spectra of the neat P3HT film and the P3HT:**SF-DPP**s films (1:1, wt/wt) which were prepared as cast from $CHCl_3$ solution and under the corresponding optimized OSCs device conditions. d) EQE curve of the optimized P3HT:**SF-DPPEH** blend film overlaid with the absorption spectra of neat P3HT and **SF-DPPEH** films.

a donor/acceptor interface. Although **SF-DPPEH**-based blends showed a relatively low quenching efficiency, the well-established network and good structural order provided a better carrier collection pathways, leading to overall enhanced device performance. These details will be shown in Section 2.6.

2.6. Film Morphology

The structural order of these new spiro-DPP compounds in pure and BHJ thin films was investigated by grazing incidence x-ray diffraction (GIXD). Shown in **Figure 6**a are the 2D diffraction patterns of the six new materials as spun and after thermal annealing. Figure 6b,c are line-cut profiles of diffraction images, which provide a quantitative understanding of the molecular packing in the solid state. The most interesting material, **SF-DPPEH**, showed poor crystalline order in the as-spun film. A very weak diffraction ring at ≈0.4 $Å^{-1}$ and a broad amorphous halo at 1.28 $Å^{-1}$ were observed. Interestingly, thermal annealing led to obvious crystallization of **SF-DPPEH**, and multiple new reflections were observed in the line-cut profile. An intense diffraction appeared at 0.38 $Å^{-1}$, corresponding to a distance of 16.5 Å, which is similar to the (100) lamellar spacing in P3HT crystals.[29] This is consequently assigned to the alkyl–alkyl spacing in **SF-DPPEH**. This molecule consists of two twisted DPP-based oligomers, and, thus, the adjacent DPP units from two molecules would interact with each other to order. The multiple diffraction peaks from 0.5 to 1.0 $Å^{-1}$ raised from the intramolecular structure of the molecule. Stronger reflections occur at 1.3–1.5 $Å^{-1}$ region in the annealed thin film, which can be attributed to the characteristic electron density variations within the DPP molecule. Additionally, a moderate diffraction peak at 1.62 $Å^{-1}$ was seen in the line-cut profiles, giving a distance of 3.9 Å, which can be attributed to the π–π stacking of DPP molecules (see Figure S7, Supporting Information). **SF-DPPC8** showed the same behavior as **SF-DPPEH**, that is, thermal annealing significantly enhanced crystallinity. A reflection is found at 0.368 $Å^{-1}$, corresponding to a distance of 17.1 Å. The slight increase in this distance for **SF-DPPC8** in comparison to **SF-DPPEH** arises from the increasing contour length of the alkyl chains. And also, there are similar diffraction patterns in the intermediate q range from 1.3–1.5 $Å^{-1}$. However, different behavior was detected for **SF-DPPC12**, where the *n*-dodecyl chains crystallized in the as spun film with an intense reflection at 0.262 $Å^{-1}$, corresponding to a distance of 24.0 Å. While, similar to short alkyl chain substituted molecules, a weak reflection at 0.375 $Å^{-1}$ also appeared. It is thus plausible to claim that the *n*-dodecyl alkyl chains adopted two

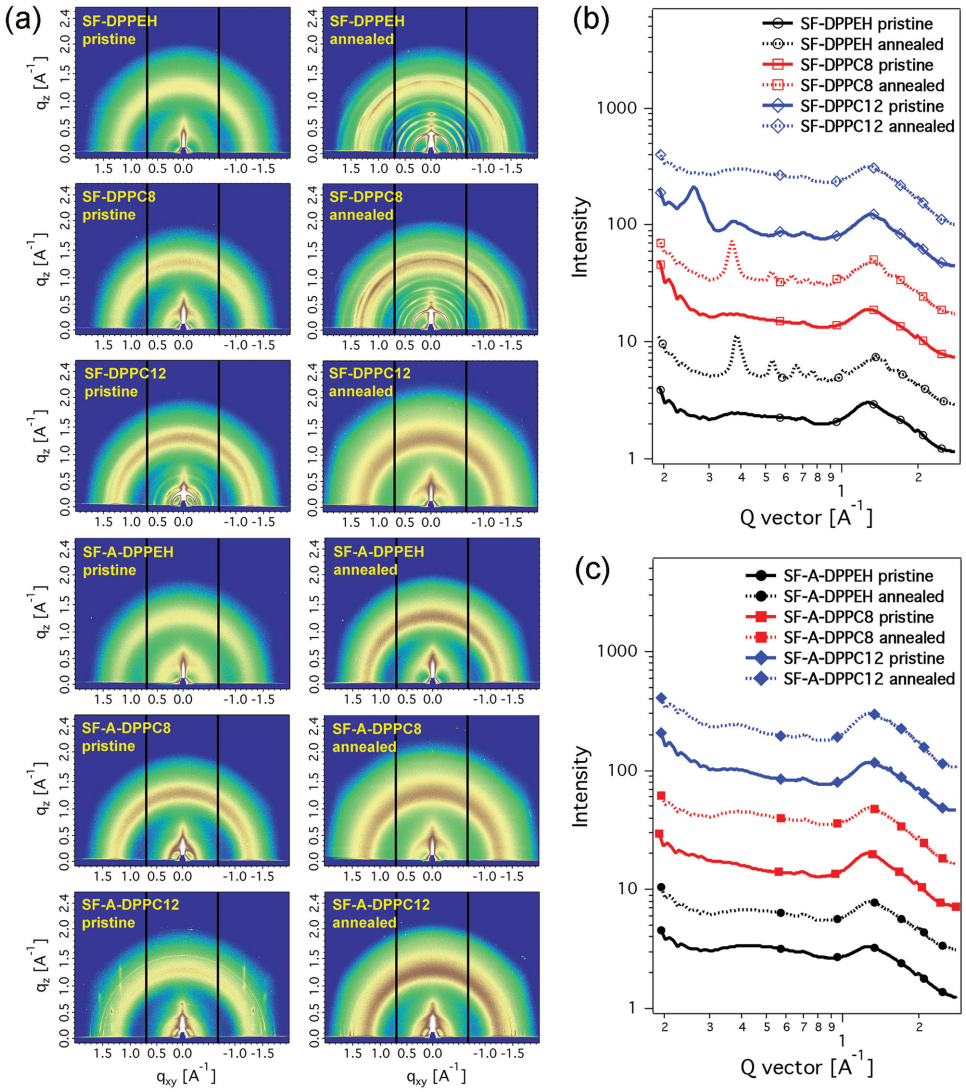

Figure 6. a) The 2D GIXD images of **SF-DPP**s and **SF-A-DPP**s thin films, pristine and annealed. b,c) 1D in-plane X-ray profiles extracted from GIXD for **SF-DPP**s and **SF-A-DPP**s, respectively.

major conformations in solid state: (1) highly stretched, which resulted in a inter DPP distance of 24 Å; and (2) frustrated that give a inter DPP distance of 16.7 Å. Thermal annealing led to the disappearance of these diffractions peaks and thus crystallinity reduced obviously.

It is apparent that the side chains greatly influence the intermolecular packing. **SF-A-DPPEH** and **SF-A-DPPC8** showed an amorphous structure in both pristine and annealed films. **SF-A-DPPC12** with long and linear substitute showed some structural order in the high q region, arising from the alkyl-chain crystallization. However, thermal annealing reduced the crystallinity in the thin film. The lack of structure order in **SF-A-DPP**s thin films would substantially reduce their electron transport characteristics which gives rise to the inferior device performance.

GIXD was also used to investigate the structural order of BHJ thin films. The processing conditions that produced best performing films were used (thermal annealing for **SF-DPP**s and **SF-A-DPPEH**, as cast for **SF-A-DPPC8** and **SF-A-DPPC12**). Shown in **Figure 7**a,b are the 2D diffraction images and line-cut profiles, respectively. In all these BHJ thin films, the diffraction from P3HT was observed with a strong π–π stacking in the out-of-plane direction, which means that P3HT favor face-on orientation. For the P3HT:**SF-DPPEH** blends, the **SF-DPPEH** crystalline structure was preserved, showing a similar pattern as seen in the pure film. The P3HT (100) at 0.38 $Å^{-1}$ with a distance of 16.5 Å is coincident with alkyl–alkyl spacing of **SF-DPPEH**. The peak intensity was the strongest in all these BHJ samples, demonstrating that P3HT highly crystallize in these BHJ films. The crystal size from a Scherrer analysis was ≈11.5 nm, corresponding to about 10 stacks. The (020) π–π stacking was observed at 1.67 $Å^{-1}$ with a crystal size of ≈4.59 nm. In the **SF-DPPC8** and **SF-DPPC12** blends, the acceptor molecules did not show good crystalline order. The crystal size in (100) direction and (020) direction were 9.23 and 4.68 nm, and 8.60 and 4.63 nm, respectively. The reduced crystallinity of the acceptor

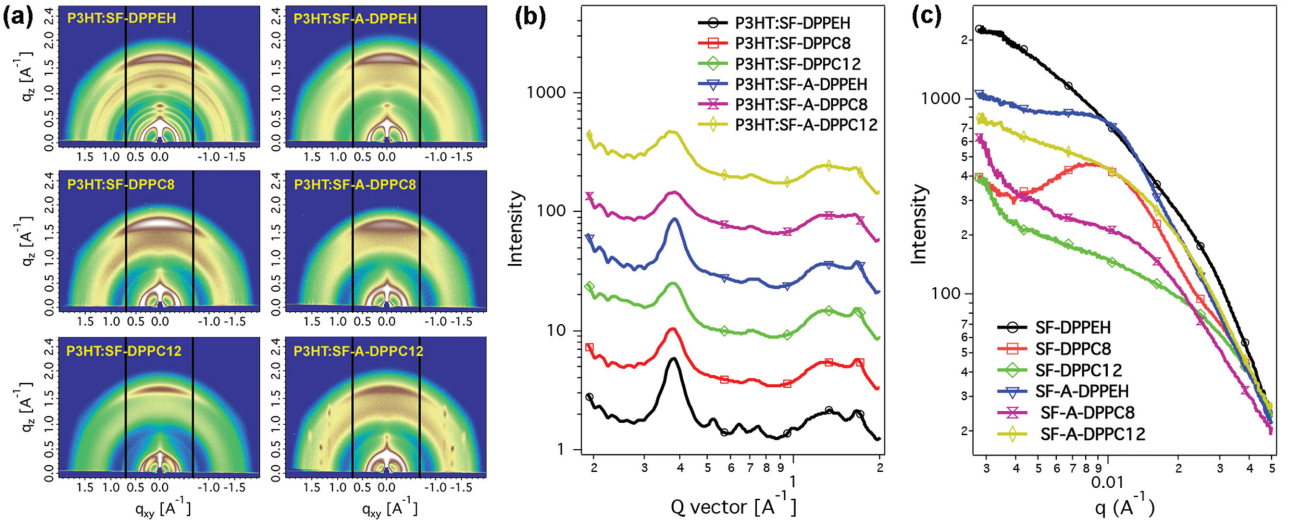

Figure 7. a) The 2D GIXD images of the optimized blend films. b) 1D in-plane X-ray profiles extracted from GIXD. c) RSoXS profiles of the six optimized blend films.

materials in the BHJ films is responsible for reduced J_{sc} in the **SF-DPPC8** and **SF-DPPC12**-based blends. This correlates well with the results obtained from the absorption of the blends. In **SF-A-DPP**-based blends, reflections from the P3HT crystals dominated the GIXD, consequently, low J_{sc} and poor PCEs were observed. Surprisingly, although the **SF-DPPC8** neat film showed behavior similar to **SF-DPPEH** with enhanced crystallinity after thermal annealing, **SF-DPPEH** obviously crystallizes but **SF-DPPC8** shows low crystallinity in the BHJ film upon thermal annealing. We suspected that the linear alkyl chain in **SF-DPPC8** could interact with hexyl chains in P3HT, which retarded **SF-DPPC8** crystallization. Whereas branching of 2-ethylhexyl group in **SF-DPPEH** blocked the interdigitation between 2-ethylhexyl group and *n*-hexyl group in P3HT, and thus repelled **SF-DPPEH** to crystallize and form more pure domains.

Recently, it has been demonstrated that side chains on electron donors and fullerenes had a significant influence on the V_{oc} through tailoring the strength of the intermolecular interactions between donor and acceptor materials in the active layer of OSCs.[30] Generally, less electronic coupling between molecules leads to reduced recombination in devices and increases the V_{oc}.[31] As discussed above, the intermolecular interaction between acceptor molecule and P3HT in P3HT:**SF-DPPEH** devices is significantly lower than in the **SF-DPPC8** and **SF-DPPC12**-based blends, which account for its distinctly higher V_{oc}. By associating the photovoltaic performance of the of P3HT:**SF-DPP** blending thin films with the molecular structure of the corresponding acceptors (**SF-DPPEH**, **SF-DPPC8**, and **SF-DPPC12**), it can be concluded that the alkyl side chains in **SF-DPP** acceptors exerted a significant influence on their photovoltaic performance through modulating the intermolecular interactions in blend films.

Resonant soft X-ray scattering (RSoXS) was used to investigate larger length scale structures in the BHJs. A photon energy of 285.4 eV that gave the best contrast was used and the results are summarized in Figure 7c. The best performing P3HT:**SF-DPPEH** blend showed an enhanced interference at ≈0.02–0.03 Å^{-1}, corresponding to a phase separated morphology with a characteristic distance of 20–30 nm. This is, more than likely, the origin of the high current in the devices. **SF-DPPC8**-based blends showed a well-defined scattering peak at ≈0.01 Å^{-1}, corresponding to a well-defined phase separated length scales of ≈60 nm. The scattering intensity of this sample was markedly lower than that of the **SF-DPPEH** blends. Consequently, the extent of phase separation was largely reduced, leading to reduced performance. The **SF-DPPC12** blends showed weak scattering with no obvious features, suggesting either a very large size scale of phase separation or phase mixing, which brought a drastic reduction in the performance. This correlated well with the results from atomic force microscopy (AFM) investigation (see Figure S8, Supporting Information). Although the **SF-A-DPP**s blends all showed interferences characteristic of a phase separated morphology (either scattering peak or hump) at ≈0.014 Å^{-1}, corresponding to a size scale of ≈45 nm, the amorphous nature of these acceptors made it hard to transport electrons and, thus, the device performance was quite poor.

Significantly, when compared the morphologies of **SF-DPPEH**-based blend film with its linear analogue, **F(DPP)$_2$B$_2$**,[13h] based blend film (**Figure 8**), one can find that the size of donor–acceptor phase separation in the former (20–30 nm) is evidently smaller than in the latter (40–60 nm), which can be proved by the improvement of J_{sc} and PCE. This indicates that the large spiro structure of **SF-DPPEH** enables a significant improvement of the morphology of blend film.

2.7. Mechanism of Phase Separation

We had shown in previous work that the thin film morphology correlated with the solar cell performance.[32] Morphology control is usually achieved by tuning the processing conditions to adjust the kinetics of phase separation and the ordering of

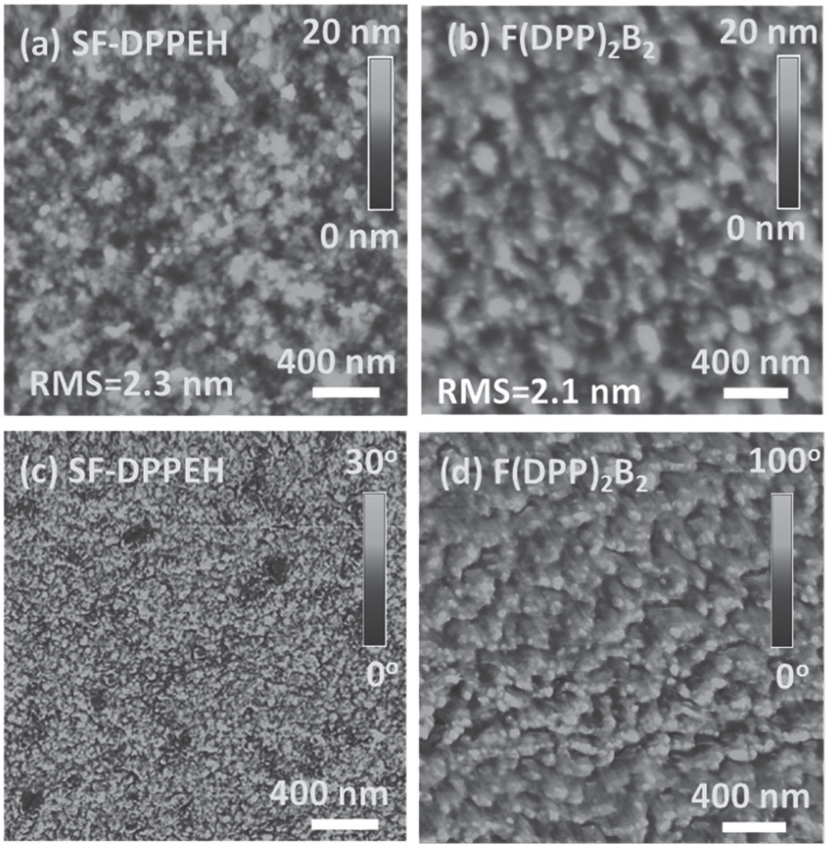

Figure 8. AFM height images a,b) and phase images c,d) of the optimized blend films: (a,c) P3HT:**SF-DPPEH** = 1:1 upon 120 °C annealing for 10 min; (b,d) P3HT:**F(DPP)$_2$B$_2$** = 1:1 upon 120 °C annealing for 10 min; e) The molecular structure of **F(DPP)$_2$B$_2$**.

the hole-transporting material. For new synthetic materials, various processing conditions should be explored to maximize their device performance. In the current case, further studies were performed on devices using the **SF-DPPEH** acceptor. The donor/acceptor ratio was fixed at 1:1, and post treatment using thermal annealing at different temperatures, as well as solvent additive methods were used to manipulate the morphology. Shown in **Table 3** are data corresponding to different device preparation conditions. Devices 1–4 were thermally annealed; Devices 5–9 were prepared using an additive. Directly casting BHJ blends from chloroform (Device 1) led to a quite poor performance with a J_{sc} of 1.04 mA cm^{-2}, a fill factor (FF) of 27.4% and PCE of 0.28%. Thermal annealing at 100 °C brought an increased J_{sc} (5.29 mA cm^{-2}) and FF (39.8%), and, thus, the PCE reached 1.81%. Increasing the annealing temperature to 120 °C enhanced these parameters and the PCE reached a maximum. Further increasing the annealing temperature to 140 °C caused a reduction in both the J_{sc} and FF and a PCE of 2.23% was obtained. In the case of additive processing, 0.4 v% of 1,8-diiooctane (DIO) and 1-chloronaphthalene (CN) were used. In both cases, the addition of additive enhanced the device performance (J_{sc} ≈ 3.5 mA cm^{-2} and FF ≈ 35%) as compared to pure chloroform processing. Thermal annealing on this additive processed thin film led to an improved morphology and increased the PCE to about 3%. These observations were quite intriguing, indicating systematic changes in the morphology.

GIXD and RSoXS measurements were carried out to explore how the nanostructures of BHJ thin films correlated with device performances and the results are shown in **Figure 9**. The as-spun BHJ thin film showed a poor crystallinity for both **SF-DPPEH** and P3HT, and an anticipated device with poor performance was found. Thermal annealing at 100 °C led to P3HT crystallization, showing both (100) and (020) reflections. The (100) crystal size was calculated to be 8.24 nm. Interestingly, increasing annealing temperature to 120 °C, **SF-DPPEH** crystallization with a structure similar to that of pure thin film was achieved. The (100) crystal size of P3HT was estimated to be 11.5 nm. Further increasing the annealing temperature to 140 °C increased the P3HT (100) crystal size to 12.4 nm and **SF-DPPEH** remained a similar packing. As for the as-spun thin film, DIO as an additive-induced P3HT crystallization and a weak **SF-DPPEH** crystallization. The (100) crystal size of P3HT was calculated to be 7.47 nm. Subsequent thermal annealing at 120 °C increased the P3HT (100) to 9.37 nm, which was slightly smaller than a direct thermal annealing at

Table 3. Summary of Device Performances for P3HT:**SF-DPPEH** (1:1) blends.

Device	Solvent	Annealing Temp. [°C]	V_{oc} [V]	J_{sc} [mA cm^{-2}]	FF	PCE [%]
1	CF	w/o	0.98	1.04	27.4	0.28
2	CF	100	0.89	5.29	39.8	1.81
3	CF	120	1.10	6.96	47.5	3.63
4	CF	140	1.04	5.40	39.6	2.23
5	CF/DIO	w/o	0.94	3.54	36.1	1.20
6	CF/DIO	120	0.97	6.50	46.5	2.93
7	CF/CN	w/o	0.88	3.56	35.5	1.11
8	CF/CN	120	1.03	7.23	42.7	3.18

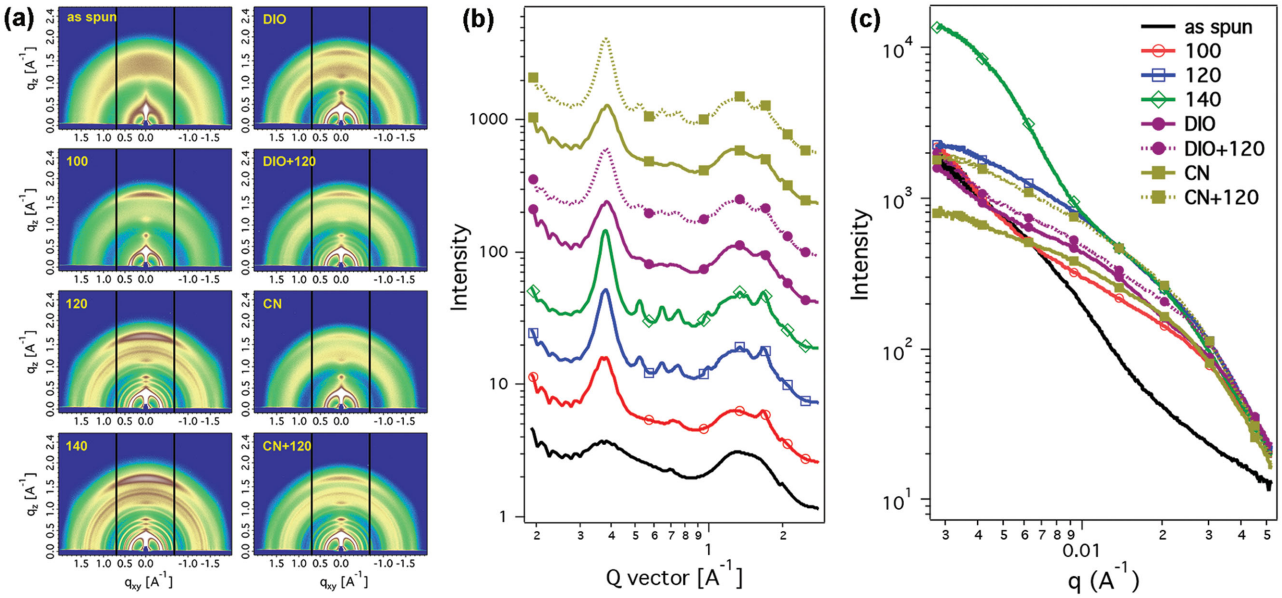

Figure 9. a) The 2D GIXD images of the P3HT:**SF-DPPEH** (1:1, wt/wt) blends with different processing conditions. b) 1D in-plane X-ray profiles extracted from GIXD. c) RSoXS profiles of above blends. Remark: The legend in (b) is same as that in (c).

the same temperature. So the relative device performance was also slightly lower. CN additive behaved quite similarly to DIO in both the as-cast and annealed thin films.

As shown in Figure 9c, for as-spun thin film casted from chloroform, the RSoXS profile showed a rapid decrease of the intensity in the high q region, indicating no phase separation at small length scales. Consequently, a poor device performance was recorded (PCE = 0.28%). Thermal annealing at 100 °C induced a phase separation at a length scale of ≈20–30 nm, as shown in the raised region of red curve. Although the crystalline order of **SF-DPPEH** was still poor under this condition, the ordered structure of P3HT and suitable phase separation led to a moderate efficiency of 1.81%. Increasing the annealing temperature to 120 °C further enhanced the intensity of RSoXS, thus a better phase separation was achieved, which, together with **SF-DPPEH** crystallization, pushed the device performance up to 3.63%. Further increasing the annealing temperature to 140 °C led to a macroscopic crystallization of P3HT, and a large size scale phase separation (>200 nm) was formed in the BHJ blends, resulting in a rapid reduction in the device performance. It should be noted that phase separation on the 20–30 nm length scale appeared to be retained in this system, which apparently plays an important role in maintaining a PCE of 2.23%. In case of the DIO additive processed thin film, thermal annealing enhanced phase separation in 20–30 nm region, as evidenced by the enhanced intensity in that region, which, combined with **SF-DPPEH** crystallization, increased device performance. For the case where CN was used as the additive, thermal annealing led to elevated scattering intensities in wide region. The as-spun and annealed films showed a similar morphology. It is obvious that the **SF-DPPEH** crystallization and the extent of phase separation are the two key factors for the enhanced performance.

The observation in this section showed that the degree of phase separation and crystallization correlated quite well with the device performance. **SF-DPPEH**, as an acceptor material, showed a maximum device performance of 3.63% PCE when combined with P3HT, reaching the common P3HT:PCBM BHJ device.[12f] As for the processing of the active layer, moderate thermal annealing appeared to significantly improve the morphology and the device performance. Although additives can also induce similar phase separated morphology, the extent of phase separation and crystallization of each component in blend films is not as good as thermally annealed blend films. Further thermal treatment, therefore, is still necessary.

3. Conclusion

We introduced an SF core-unit to generate spiro-DPPs-based nonfullerene acceptors. The effects of substituted alkyl side chains on molecular packing, crystallinity, and BHJ film morphology were studied. The unique X-shaped molecular structure resulting from the spiro linkage imparted high solubility and suppressed aggregation. In the material design, we found that small perturbations of the chemical structure, for example, the choice of different side chains and C–C single bond or C–C triple bond connection, led to quite different physical properties. In BHJ blends, **SF-DPPEH** crystallizes well after thermal annealing, while **SF-DPPC8** and **SF-DPPC12** showed low crystallinity. Further, the branched 2-ethylhexyl group provided **SF-DPPEH** interacted less with P3HT, leading to an increased in the V_{oc}. Together with moderate crystallization of the acceptors, the nanoscaled phase separation (20–30 nm) and, thus, the less geminate recombination pushed the device performance of P3HT:**SF-DPPEH** blends up to 3.63%. This result showed that, based on the alkyl side chains of donor materials, the choice of alkyl side chains substituting on acceptors is a key in achieving a good morphology and high PCE. Thermal annealing was found to be more effective in crystallizing these nonfullerene

acceptors than additives. Most importantly, these results demonstrate that using spiro linkage to construct *n*-type molecules with cruciform X-shape is a useful strategy for designing high-performance nonfullerene OSC acceptors.

Supporting Information

Supporting Information is available from the Wiley Online Library or from the author.

Acknowledgements

X.-F.W. and W.-F.F. contributed equally to this work. This work was supported by the National Natural Science Foundation of China (No. 21372057). F.L. and T.P.R. were supported by Polymer-Based Materials for Harvesting Solar Energy (PHaSE), an Energy Frontier Research Center funded by the U.S. Department of Energy, Office of Basic Energy Sciences under Award No. DE-SC0001087. Portions of this research were carried out at beamline 7.3.3 and 11.0.1.2 at the Advanced Light Source, and Molecular Foundary, Lawrence Berkeley National Laboratory, which was supported by the DOE, Office of Science, and Office of Basic Energy Sciences. The authors also thank Dr. C. W. Hao (Hang Zhou Normal University) for the helpful discussion.

Received: June 12, 2015
Revised: August 1, 2015
Published online: August 27, 2015

[1] a) Y.-J. Cheng, S.-H. Yang, C.-S. Hsu, *Chem. Rev.* **2009**, *109*, 5868; b) Y. Li, *Acc. Chem. Res.* **2011**, *45*, 723; c) G. Li, R. Zhu, Y. Yang, *Nat. Photonics* **2012**, *6*, 153; d) Z. He, H. Wu, Y. Cao, *Adv. Mater.* **2014**, *26*, 1006; e) L. Ye, S. Zhang, L. Huo, M. Zhang, J. Hou, *Acc. Chem. Res.* **2014**, *47*, 1595; f) Y. Liang, L. Yu, *Acc. Chem. Res.* **2010**, *43*, 1227.

[2] a) J. E. Coughlin, Z. B. Henson, G. C. Welch, G. C. Bazan, *Acc. Chem. Res.* **2014**, *47*, 257; b) Y. Li, Q. Guo, Z. Li, J. Pei, W. Tian, *Energy Environ. Sci.* **2010**, *3*, 1427; c) B. Walker, C. Kim, T. Q. Nguyen, *Chem. Mater.* **2011**, *23*, 470; d) Y. Lin, X. Zhan, Y. Li, *Chem. Soc. Rev.* **2012**, *41*, 4245; e) Y. Chen, X. Wan, G. Long, *Acc. Chem. Res.* **2013**, *46*, 2645.

[3] a) J. Bloking, T. Giovenzana, A. T. Higgs, A. J. Ponec, E. T. Hoke, K. Vandewal, S. Ko, Z. Bao, A. Sellinger, M. D. McGehee, *Adv. Energy Mater.* **2014**, *4*, 1301426; b) V. D. Mihailetchi, J. K. J. van Duren, P. W. M. Blom, J. C. Hummelen, R. A. J. Janssen, J. M. Kroom, M. T. Rispens, W. J. H. Verhees, M. M. Wienk, *Adv. Funct. Mater.* **2003**, *13*, 43; c) Y. He, Y. Li, *Phys. Chem. Chem. Phys.* **2011**, *13*, 1970; d) R. D. Pensack, C. Guo, K. Vakhshouri, E. D. Gomez, J. B. Asbury, *J. Phys. Chem. C.* **2012**, *116*, 482; e) B. M. Savoie, A. Rao, A. A. Bakulin, S. Gelinas, B. Movaghar, R. H. Friend, T. J. Marks, M. A. Ratner, *J. Am. Chem. Soc.* **2014**, *136*, 2876.

[4] a) W. Ma, J. R. Tumbleston, M. Wang, E. Gann, F. Huang, H. Ade, *Adv. Energy Mater.* **2013**, *3*, 864; b) N. D. Treat, M. A. Brady, G. Smith, M. F. Toney, E. J. Kramer, C. J. Hawker, M. L. Chabinyc, *Adv. Energy Mater.* **2011**, *1*, 82; c) J. Peet, M. L. Senatore, A. J. Heeger, G. C. Bazan, *Adv. Mater.* **2009**, *21*, 1521.

[5] a) H. C. Hesse, J. Weickert, C. Hundschell, X. Feng, K. Müllen, B. Nickel, A. J. Mozer, L. Schmidt-Mende, *Adv. Energy Mater.* **2011**, *1*, 861; b) M. M. Wienk, J. M. Kroon, W. J. H. Verhee, J. Knol, J. C. Hummelen, P. A. van Hal, R. A. J. Janssen, *Angew. Chem. Int. Ed.* **2003**, *42*, 3371.

[6] a) Y. He, H.-Y. Chen, J. Hou, Y. Li, *J. Am. Chem. Soc.* **2010**, *132*, 1377; b) C. J. Brabec, A. Cravino, D. Meissner, N. S. Sariciftci, T. Fromherz, M. T. Rispens, L. Sanchez, J. C. Hummelen, *Adv. Funct. Mater.* **2001**, *11*, 374.

[7] A. Anctil, C. W. Babbitt, R. P. Raffaelle, B. J. Landi, *Environ. Sci. Technol.* **2011**, *45*, 2353.

[8] a) Y. Lin, X. Zhan, *Mater. Horiz.* **2014**, *1*, 470; b) C. L. Chochos, N. Tagmatarchis, V. G. Gregoriou, *RSC Adv.* **2013**, *3*, 7160; c) A. Fachetti, *Mater. Today* **2013**, *16*, 123; d) Y. Lin, X. Zhan, Y. Li, *Chem. Soc. Rev.* **2012**, *41*, 4245; e) A. F. Eftaiha, J.-P. Sun, I. G. Hill, G. C. Welch, *J. Mater. Chem. A* **2014**, *2*, 1201; f) P. Sonar, J. P. F. Lim, K. L. Chan, *Energy Environ. Sci.* **2011**, *4*, 1558.

[9] a) X. Zhan, Z. Tan, B. Domercq, Z. An, X. Zhang, S. Barlow, Y. Li, D. Zhu, B. Kippelen, S. R. Marder, *J. Am. Chem. Soc.* **2007**, *129*, 7246; b) Y. Zhou, T. Kurosawa, W. Ma, Y. Guo, L. Fang, K. Vandewal, Y. Diao, C. Wang, Q. Yan, J. Reinspach, J. Mei, A. L. Appleton, G. I. Koleilat, Y. Gao, S. C. B. Mannsfeld, A. Salleo, H. Ade, D. Zhao, Z. Bao, *Adv. Mater.* **2014**, *26*, 3767; c) T. W. Holcombe, C. H. Woo, D. F. J. Kavulak, B. C. Thompson, J. M. J. Frechet, *J. Am. Chem. Soc.* **2009**, *131*, 14160; d) W. Li, W. S. C. Roelofs, M. Turbiez, M. M. Wienk, R. A. J. Janssen, *Adv. Mater.* **2014**, *26*, 3304; e) I. Jung, W.-Y. Lo, J. Jang, W. Chen, D. Zhao, E. S. Landry, L. Lu, D. V. Talapin, L. Yu, *Chem. Mater.* **2014**, *26*, 3450; f) C. Mu, P. Liu, W. Ma, K. Jiang, J. Zhao, K. Zhang, Z. Chen, Z. Wei, Y. Yi, J. Wang, S. Yang, F. Huang, A. Facchetti, H. Ade, H. Yan, *Adv. Mater.* **2014**, *26*, 7224; g) Y.-J. Hwang, T. Earmme, B. A. E. Courtright, F. N. Eberle, S. A. Jenekhe, *J. Am. Chem. Soc.* **2015**, *137*, 4424; h) E. Zhou, J. Cong, Q. Wei, K. Tajima, C. Yang, K. Hashimoto, *Angew. Chem. Int. Ed.* **2011**, *50*, 2799.

[10] a) T. Zhou, T. Jia, B. Kang, F. Li, M. Fahlman, Y. Wang, *Adv. Energy Mater.* **2011**, *1*, 431; b) Y. Shu, Y.-F. Lim, Z. Li, B. Purushothaman, R. Hallani, J. Kim, S. R. Parkin, G. G. Malliaras, J. E. Anthony, *Chem. Sci.* **2011**, *2*, 363; c) Y. Lin, Z. Zhang, H. Bai, J. Wang, Y. Yao, Y. Li, D. Zhu, X. Zhan, *Energy Environ. Sci.* **2015**, *8*, 610; d) C. B. Nielsen, E. Voroshazi, S. Holliday, K. Cnops, B. P. Rand, I. McCulloch, *J. Mater. Chem. A* **2013**, *1*, 73; e) G. D. Sharma, M. Anil Reddy, D. V. Ramana, M. Chandrasekharam. *RSC Adv.* **2014**, *4*, 33279.

[11] a) X. Zhang, Z. Lu, L. Ye, C. Zhan, J. Hou, S. Zhang, B. Jiang, Y. Zhao, J. Huang, S. Zhang, Y. Liu, Q. Shi, Y. Liu, J. Yao, *Adv. Mater.* **2013**, *25*, 5791; b) A. Sharenko, C. M. Proctor, T. S. van der Poll, Z. B. Henson, T.-Q. Nguyen, G. C. Bazan. *Adv. Mater.* **2013**, *25*, 4403; c) W. Jiang, L. Ye, X. Li, C. Xiao, F. Tan, W. Zhao, J. Hou, Z. Wang, *Chem. Commun.* **2014**, *50*, 1024; d) H. Li, T. Earmme, G. Ren, A. Saeki, S. Yoshikawa, N. M. Murari, S. Subramaniyan, M. J. Crane, S. Seki, S. A. Jenekhe, *J. Am. Chem. Soc.* **2014**, *136*, 14589; e) S. Rajaram, R. Shivanna, S. Kandappa, K. S. Narayan. *J. Phys. Chem. Lett.* **2012**, *3*, 2405; f) Y. Zheng, Y. Dai, Y. Zhou, J. Wang, J. Pei, *Chem. Commun.* **2014**, *50*, 1591; g) T. V. Pho, F. M. Toma, M. L. Chabinyc, F. Wudl, *Angew. Chem. Int. Ed.* **2013**, *52*, 1446; h) G. Ren, E. Ahmed, S. A. Jenekhe, *J. Mater. Chem.* **2012**, *22*, 24373; i) O. K. Kwon, J. Park, D. W. Kim, S. K. Park, S. Y. Park, *Adv. Mater.* **2015**, *27*, 1951; j) P. E. Hartnett, A. Timalsina, H. S. S. R. Matte, N. Zhou, X. Guo, W. Zhao, A. Facchetti, R. P. H. Chang, M. C. Hersam, M. R. Wasielewski, T. J. Marks, *J. Am. Chem. Soc.* **2014**, *136*, 16345; k) H. Li, T. Earmme, S. Subramaniyan, S. A. Jenekhe, *Adv. Energy Mater.* **2015**, *5*, 1402041; l) Y. Cai, L. Huo, X. Sun, D. Wei, M. Tang, Y. Sun. *Adv. Energy Mater.* **2015**, *5*, 1500032.

[12] a) P. E. Schwenn, K. Gui, A. M. Nardes, K. B. Krueger, K. H. Lee, K. Mutkins, H. Rubinstein-Dunlop, P. E. Shaw, N. Kopidakis, P. L. Burn, P. Meredith, *Adv. Energy Mater.* **2011**, *1*, 73; b) C. H. Woo, T. W. Holcombe, D. A. Unruh, A. Sellinger, J. M. J. Frechet, *Chem. Mater.* **2010**, *22*, 1673; c) J. T. Bloking, X. Han, A. T. Higgs, J. P. Kastrop, L. Pandey, J. E. Norton, C. Risko, C. E. Chen, J.-L. Bredas, M. D. McGehee, A. Sellinger, *Chem. Mater.* **2011**, *23*, 5484; d) Y. Lin, H. Wang, Y. Li, D. Zhu, X. Zhan, *J. Mater.*

Chem. A **2013**, *1*, 14627; e) J. D. Douglas, Mark. S. Chen, J. R. Niskala, O. P. Lee, A. T. Yiu, E. P. Young, J. M. J. Fréchet, *Adv. Mater.* **2014**, *26*, 4313; f) S. Holliday, R. S. Ashraf, C. B. Nielsen, M. Kirkus, J. A. Röhr, C.-H. Tan, E. Collado-Fregoso, A.-C. Knall, J. R. Durrant, J. Nelson, I. McCulloch, *J. Am. Chem. Soc.* **2015**, *137*, 898.

[13] a) P. Sonar, G.-M. Ng, T. T. Lin, A. Dodabalapur, Z.-K. Chen, *J. Mater. Chem.* **2010**, *20*, 3626; b) B. P. Karsten, J. C. Bijleveld, R. A. J. Janssen, *Macromol. Rapid Commun.* **2010**, *31*, 1554; c) A. M. Raynor, A. Gupta, H. Patil, A. Bilicc, S. V. Bhosale, *RSC Adv.* **2014**, *4*, 57635; d) H. Patil, W. Zu, A. Gupta, V. Chellappan, A. Bilic, P. Sonar, A. Rananaware, S. V. Bhosalee, *Phys. Chem. Chem. Phys.* **2014**, *16*, 23837; e) H. Patil, A. Gupta, A. Bilic, S. V. Bhosale, *Tetrahedron Lett.* **2014**, *55*, 4430; f) Y. Lin, Y. Li, X. Zhan, *Adv. Energy Mater.* **2013**, *3*, 724; g) Y. Yang, G. Zhang, C. Yu, C. He, J. Wang, X. Chen, J. Yao, Z. Liu, D. Zhang, *Chem. Commun.* **2014**, *50*, 9939; h) H. Shi, W. Fu, M. Shi, J. Ling, H. Chen, *J. Mater. Chem. A* **2015**, *3*, 1902.

[14] a) Y. Kim, C. Song, S. Moonc, E. Lim. *Chem. Commun.* **2014**, *50*, 8235; b) Z. Mao, W. Senevirathna, J. Liao, J. Gu, S. V. Kesava, C. Guo, E. D. Gomez, G. Sauvé, *Adv. Mater.* **2014**, *26*, 6290.

[15] a) Y. Liu, C. Mu, K. Jiang, J. Zhao, Y. Li, L. Zhang, Z. Li, J. Yuk, L. Lai, H. Hu, T. Ma, R. Hu, D. Yu, X. Huang, B. Tang, H. Yan, *Adv. Mater.* **2015**, *6*, 1015; b) Q. Yan, Y. Zhou, Y. Zheng, J. Pei, D. Zhao, *Chem. Sci.* **2013**, *4*, 4389.

[16] a) X. Zhang, J. Yao, C. Zhan, *Chem. Commun.* **2015**, *51*, 1058; b) Z. Lu, B. Jiang, X. Zhang, A. Tang, L. Chen, C. Zhan, J. Yao, *Chem. Mater.* **2014**, *26*, 2907; c) L. Ye, W. Jiang, W. Zhao, S. Zhang, D. Qian, Z. Wang, J. Hou, *Small* **2014**, *10*, 4658; d) Y. Zhong, M. T. Trinh, R. Chen, W. Wang, P. P. Khlyabich, B. Kumar, Q. Xu, C. Nam, M. Y. Sfeir, C. Black, M. L. Steigerwald, Y.-L. Loo, S. Xiao, F. Ng, X.-Y. Zhu, C. Nuckolls, *J. Am. Chem. Soc.* **2014**, *136*, 15215; e) Y. Zang, C.-Z. Li, C.-C. Chueh, S. T. Williams, W. Jiang, Z.-H. Wang, J.-S. Yu, A. K.-Y. Jen, *Adv. Mater.* **2014**, *26*, 5708; f) Y. Zhong, M. T. Trinh, R. Chen, W. Wang, P. P. Khlyabich, B. Kumar, Q. Xu, C.-Y. Nam, M. Y. Sfeir, C. Black, M. L. Steigerwald, Y.-L. Loo, S. Xiao, F. Ng, X.-Y. Zhu, C. Nuckolls, *J. Am. Chem. Soc.* **2014**, *136*, 15215; g) H. Li, Y.-J. Hwang, B. A. E. Courtright, F. N. Eberle, S. Subramaniyan, S. A. Jenekhe, *Adv. Mater.* **2015**, *27*, 3266.

[17] X. Zhan, A. Facchetti, S. Barlow, T. J. Marks, M. A. Ratner, M. R. Wasielewski, S. R. Marder, *Adv. Mater.* **2011**, *23*, 268.

[18] a) Y. Lin, P. Cheng, Y. Li, X. Zhan, *Chem. Commun.* **2012**, *48*, 4773; b) Y. Wang, J. Wang, J. Hou, Y. Li, D. Zhu, X. Zhan, *Adv. Mater.* **2014**, *26*, 5137.

[19] a) S. Liu, C. Wu, C. Li, S. Liu, K.-H. Wei, H. Chen, A. K.-Y. Jen, *Adv. Sci.* **2015**, *2*, 1500014; b) W. Chen, X. Yang, G. Long, X. Wan, Y. Chen, Q. Zhang, *J. Mater. Chem. C* **2015**, *3*, 4698.

[20] a) Y. Qiao, Y. Guo, C. Yu, F. Zhang, W. Xu, Y. Liu, D. Zhu, *J. Am. Chem. Soc.* **2012**, *134*, 4084; b) J. Lee, A.-R. Han, H. Yu, T. Shin, C. Yang, J. Oh. *J. Am. Chem. Soc.* **2013**, *135*, 9540; c) J. D. Yuen, J. Fan, J. Seifter, B. Lim, R. Hufschmid, A. J. Heeger, F. Wudl, *J. Am. Chem. Soc.* **2011**, *133*, 20799; d) C. Kanimozhi, N. Yaacobi-Gross, K. W. Chou, A. Amassian, T. D. Anthopoulos, S. Patil, *J. Am. Chem. Soc.* **2012**, *134*, 16532.

[21] a) T. P. I. Saragi, T. Spehr, A. Siebert, T. Fuhrmann-Lieker, J. Salbeck, *Chem. Rev.* **2007**, *107*, 1011; b) S. Ma, Y. Fu, D. Ni, J. Mao, Z. Xie, G. Tu, *Chem. Commun.* **2012**, *48*, 11847.

[22] J. Zhao, Y. Li, H. Lin, Y. Liu, K. Jiang, C. Mu, T. Ma, J. Y. L. Lai, H. Yan, *Energy Environ. Sci.* **2015**, *8*, 520.

[23] N. D. Eisenmenger, G. M. Su, G. C. Welch, C. J. Takacs, G. C. Bazan, E. J. Kramer, M. L. Chabinyc, *Chem. Mater.* **2013**, *25*, 1688.

[24] M. Jung, Y. Yoon, J. H. Park, W. Cha, A. Kim, J. Kang, S. Gautam, D. Seo, J. H. Cho, H. Kim, J. Y. Choi, K. H. Chae, K. Kwak, H. J. Son, M. J. Ko, H. Kim, D.-K. Lee, J. Y. Kim, D. H. Choi, B. Kim, *ACS Nano* **2014**, *8*, 5988.

[25] a) H. Bürckstümmer, A. Weissenstein, D. Bialas, F. Würthner, *J. Org. Chem.* **2011**, *76*, 2426; b) A. B. Tamayo, M. Tantiwiwat, B. Walker, T.-Q. Nguyen. *J. Phys. Chem. C.* **2008**, *112*, 15543; c) H. Zhong, J. Smith, S. Rossbauer, A. J. P. White, T. D. Anthopoulos, M. Heeney, *Adv. Mater.* **2012**, *24*, 3205.

[26] Q. Shi, P. Cheng, Y. Li, X. Zhan, *Adv. Energy Mater.* **2012**, *2*, 63.

[27] B. Jiang, X. Zhang, C. Zhan, Z. Lu, J. Huang, X. Ding, S. He, J. Yao, *Polym. Chem.* **2013**, *4*, 4631.

[28] a) D. Credgington, R. Hamilton, P. Atienzar, J. Nelson, J. R. Durrant, *Adv. Funct. Mater.* **2011**, *21*, 2744; b) B. Qi, J. Wang, *J. Mater. Chem.* **2012**, *22*, 24315; c) P. P. Khlyabich, A. E. Rudenko, R. A. Street, B. C. Thompson, *ACS Appl. Mater. Interfaces* **2014**, *6*, 9913.

[29] M. Brinkmann, J. C. Wittmann, *Adv. Mater.* **2006**, *18*, 860.

[30] a) W. J. Potscavage, S. Yoo, B. Kippelen, *Appl. Phys. Lett.* **2008**, *93*, 193308; b) M. D. Perez, C. Borek, S. R. Forrest, M. E. Thompson, *J. Am. Chem. Soc.* **2009**, *131*, 9281; c) L. Yang, H. Zhou, W. You, *J. Phys. Chem. C.* **2010**, *114*, 16793; d) L. Yang, J. R. Tumbleston, H. Zhou, H. Ade, W. You, *Energy Environ. Sci.* **2013**, *6*, 316; e) S. Yamamoto, A. Orimo, H. Ohkita, H. Benten, S. Ito, *Adv. Energy Mater.* **2012**, *2*, 229.

[31] K. N. Winzenberg, P. Kemppinen, F. H. Scholes, G. E. Collis, Y. Shu, T. B. Singh, A. Bilic, C. M. Forsythb, S. E. Watkins, *Chem. Commun.* **2013**, *49*, 6307.

[32] a) Q.-C. Yu, W.-F. Fu, J.-H. Wan, X.-F. Wu, M.-M. Shi, H.-Z. Chen. *ACS Appl. Mater. Interfaces* **2014**, *6*, 5798; b) H. Wang, F. Liu, L. Bu, J. Gao, C. Wang, W. Wei, T. P. Russell, *Adv. Mater.* **2013**, *25*, 6519; c) F. Liu, C. Wang, J. K. Baral, L. Zhang, J. J. Watkins, A. L. Briseno, T. P. Russell, *J. Am. Chem. Soc.* **2013**, *135*, 19248.